Materials Today • Volume xxx, Number xx • xxxx 2020 RESEARCH

ELSEVIER

RESEARCH: Original Research

# 1D hypo-crystals: A novel concept for the crystallization of stereo-irregular polymers

Jae Hyun Sim [1], Sangwon Eom [2], Sangheon Lee [2], Changjun Oh [2], Minhwan Lee [3], Seulwoo Kim [3], Won Bo Lee [3], Jungju Ryu [2], Daewon Sohn [2], Hoeil Chung [2], Jinho Hyon [4], Cheolmin Park [5], Edwin L. Thomas [4], Youngjong Kang [1,2,*]

[1] Institute of Nano Science and Technology, Hanyang University, 222 Wangsimni-Ro, Seongdong-gu, Seoul 04763, South Korea
[2] Department of Chemistry, Hanyang University, 222 Wangsimni-ro, Seongdong-gu, Seoul, 04763, South Korea
[3] School of Chemical and Biological Engineering, and Institute of Chemical Processes, Seoul National University, 1 Gwanak-ro, Gwanak-gu, Seoul 08826, South Korea
[4] Department of Materials Science and Nano Engineering, Rice University, Houston, TX 77005, USA
[5] Department of Materials Science and Engineering, Yonsei University, 50 Yonsei-ro, Seodaemun-gu, Seoul 03722, South Korea

**It has been believed that stereo-irregular polymers hardly form crystalline structure because of the deficient ordering along the backbone direction. Here we show the crystallization of atactic polymers by rapid thermal quenching of polymers co-melted with a chain-stretching agent. To this end, crystalline PMMAs (hc-PMMAs) are prepared from stereo-irregular atactic-PMMAs ($M_n$ = 35–1500 kg/-mol) as well as stereo-regular isotactic- and syndiotactic-PMMAs by rapid quenching of molten PMMA/benzoic acid (BA) solutions. BA acts as a chain-stretching agent. PMMA chains are elongated up to 60% of their contour length when they are co-melted with BA. The preferential hydrogen bonding between PMMA and BA compensates the conformational entropy loss of PMMA chains in molten PMMA/BA solutions. Upon quenching, PMMA chains are further stretched because of the large tensile stress induced by the sudden temperature drop and because of mechanical squeezing by concomitant directional crystallization of anisotropic lath-like BA crystals. After sublimation of BA, the PMMA shows a clear melting transition: $T_m$ = 276–283 °C for hc-*s*-PMMA and 293–306 °C for hc-*a*-PMMA. Unlike other conventional crystals having 3D crystallinity, hc-PMMAs exhibits 1D crystallinity due to ordered lateral packing between chains ($d$ = ~4.3 Å) which is independent on the tacticity while the packing is amorphous-like for the other two directions. For the reason of the reduced dimensionality in crystallinity, we named the crystalline PMMA as 1D hypo-crystalline PMMA (hc-PMMA). Because of their high 1D crystallinity (55–65%), hc-PMMAs exhibit the storage modulus ($E'$) enhanced by 20 times comparing with those of pristine PMMA.**

## Introduction

Polymer crystallization is intriguing from both the aspect of fundamental science and of engineering. While a huge number of research activities on the crystallizable natural and synthetic polymers have been delivered for a long time [1–5], polymer crystallization is still challenging and is still far from completely understood. This is mainly because polymer crystallization does not follow simple thermodynamic rules, but is instead normally

* Corresponding author.
*E-mail address:* Kang, Y. (youngjkang@hanyang.ac.kr)

 https://doi.org/10.1016/j.mattod.2020.05.003



Please cite this article in press as: J.H. Sim et al., Materials Today (2020), https://doi.org/10.1016/j.mattod.2020.05.003

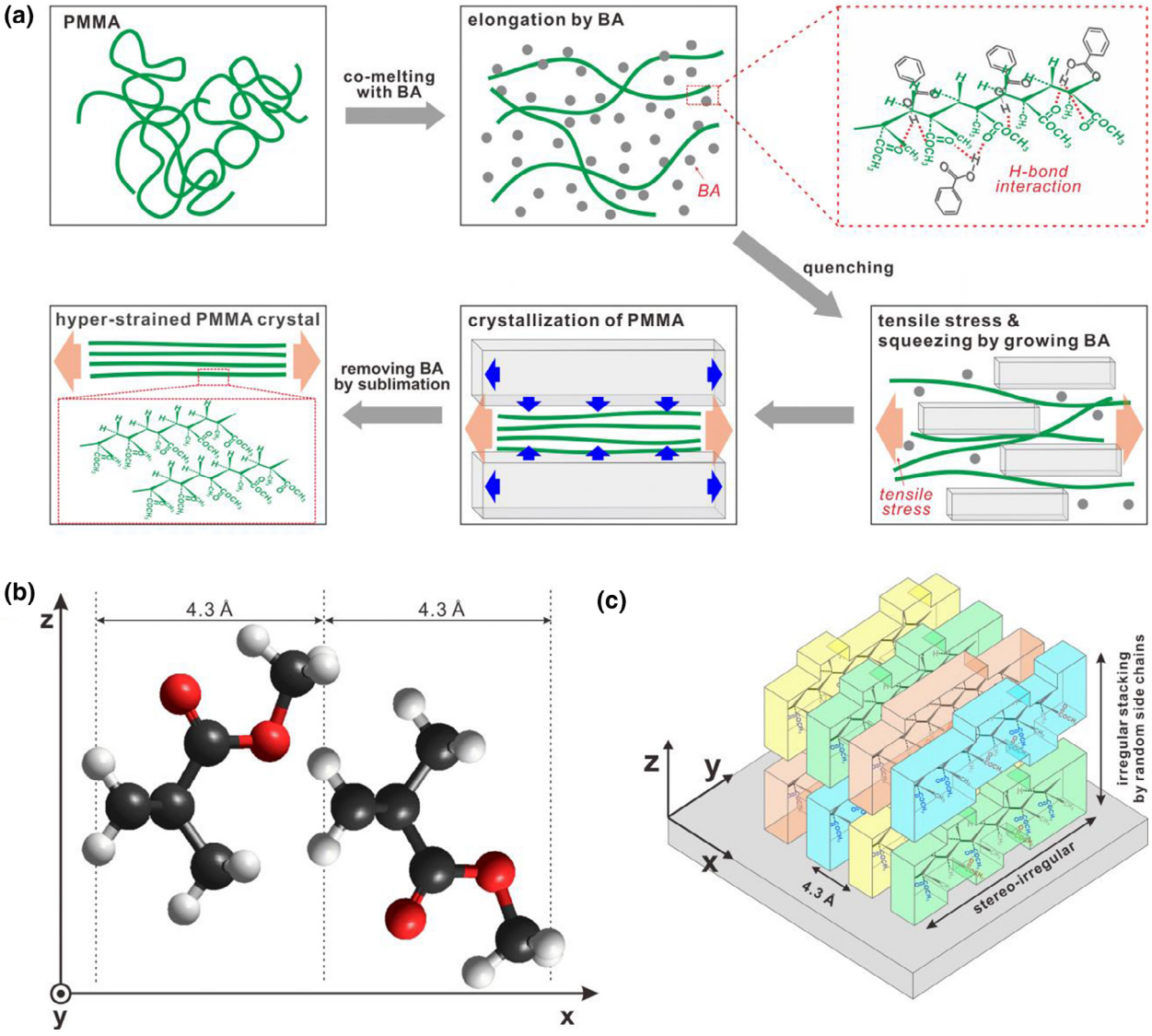


**SCHEME 1**

(a) Preparation of hc-PMMA by quenching from PMMA/BA molten solution. (b) The molecular structure of PMMA viewing along the stretched backbone axis. (c) The schematic illustration of hc-*a*-PMMA structure. The different color and box shape represent different stereo-regularity of side groups.

kinetically controlled and usually results in a non-equilibrium partially crystalline state. Furthermore, crystallization becomes more difficult for high molecular weight polymers because the melt diffusion of polymer chains by reptation decreases dramatically with molecular weight ($D \sim M^{-2}$). Additionally, polymer crystallization is hindered by the stereo-irregularity of chains. Thus, most polymer crystals have been prepared by using polymers having no stereo-center or by using highly stereo-regular ones (tacticity $\geq$~95%). However some of atactic polymers such as poly(vinyl chloride) (PVC) and polyacrylonitrile (PAN) exhibited the weak crystallinity (<10%) by forming the paracrystalline microdomains where there is only short- or mid-range ordering in their lattice but lacking crystal-like long-range ordering [6–8]. The shape–emulation model explained how those two atactic polymers can form comparatively high levels of order [9,10], but yet not explain well why other atactic vinyl polymers including poly(methyl methacrylate) (PMMA) and polystyrene (PS) cannot form crystals.

In order to crystallize, chains must assume extended conformations, however, the chains quickly fluctuate back to their coiled state before they can effectively interact with other extended chains to form crystalline structure [11–16]. Hence typical polymer crystals form spherulites consisting of folded lamellae rather than of extended chains. In this case, the lamellar thickness is much smaller than the contour length of polymer [17,18]. As a way of detouring such thermodynamic and kinetic constraints, crystallization by mechanical stretching is often adopted. This utilizes the fact that the elongated polymer chains tend to crystallize due to the large loss of conformational entropy during stretching is compensated by the enthalpic gain of crystal formation [19]. These considerations are well consistent with the extensive observation that many of elastomers which don't readily crystallize from melt, form crystals (crystallinity ~35%) easily when highly stretched [20]. Similarly, fibers or shish-kebab structures under uniaxial extensional flow was utilized for highly aligned liquid crystalline polymers [21–24].



Please cite this article in press as: J.H. Sim et al., Materials Today (2020), https://doi.org/10.1016/j.mattod.2020.05.003

RESEARCH: Original Research

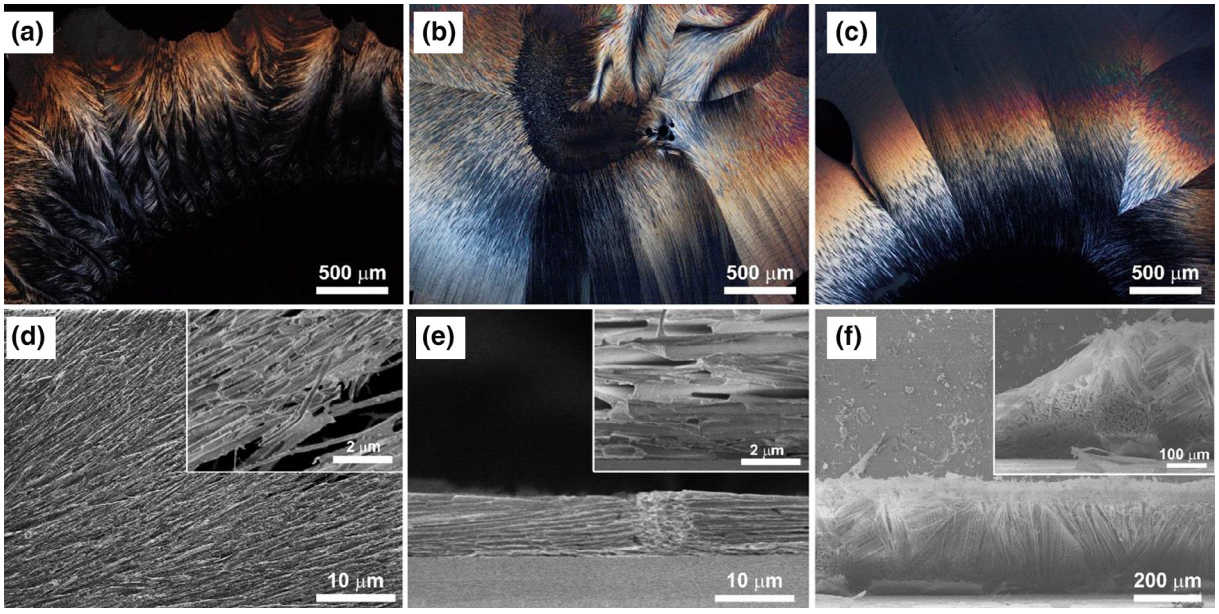


**FIGURE 1**

(a–c) Polarized optical microscopy (POM) images of hc-PMMA films prepared with (a) *i*-PMMA ($M_n$ = 37.2 kg/mol), (b) *s*-PMMA ($M_n$ = 35 kg/mol) and (c) *a*-PMMA ($M_n$ = 35 kg/mol). (d–f) SEM images of as-prepared hc-*s*-PMMA ($M_n$ = 35 kg/mol) films. (d) Top-view images showing laterally aligned microfibrils. (e) Cross-section of thin film area. Most of fibrils were laterally aligned in thin film area (<20 μm), however (f) both vertically and laterally aligned fibrils were found in thick film area (>100 μm).

PMMA which has three isomeric forms (isotactic, syndiotactic and atactic) is typically a glassy polymer. Crystallization of PMMA is very difficult because its high monomeric friction slows down crystallization rate and the flexible alpha methyl and methyl ester side groups hinder packing of PMMA chains [25]. Examples of PMMA crystallization are mostly the mechanically stretched isotactic PMMA (*i*-PMMA) films. Since Fox *et al*. first reported the crystallization of *i*-PMMA, it has been known that only highly stereoregular *i*-PMMAs ($i > 98\%$) develop crystalline structures by forming double helices [26–29]. Crystallization of other syndiotactic (*s*-PMMA) or stereo-irregular PMMA (*a*-PMMA), however, has not been yet reported.

In this work, we report crystallization of stereo-irregular *a*-PMMAs as well as stereo-regular *i*- and *s*-PMMAs by very fast thermal quenching of PMMA chains co-melted with an organic crystal herein called a 'chain-stretching agent' (benzoic acid in this work) (Scheme 1). The terminology, chain-stretching agent was used because it leads to elongate PMMA chains in molten state and accordingly decreases conformational entropy of the chains. To our surprise, we found using SAXS that PMMA chains were highly elongated up to 60% of their contour length when they were co-melted with benzoic acid (BA) with a concentration of 5 wt%, and the subsequent co-crystallization by quenching to −196 °C, far below the glass transition temperature ($T_g$) of PMMA led to the formation of PMMA crystals exhibiting a surprisingly high degree of crystallinity (55–65%). Their melting transition was clearly observed around at 270–290 °C, and their storage modulus ($E'$) was dramatically enhanced by ~20 times at room temperature with that of unprocessed PMMA. To our understanding, this is the first report on the crystallization of stereo-irregular PMMAs. Furthermore, such crystallization by quenching is contradictory to the common knowledge that vitrification occurs rather than crystal growth with increase of cooling rate since there is insufficient time for molecular rearrangements required for orderly packing of extended, parallel chains. We believe that the crystallization originates from the elongation of PMMA chains by the chain-stretching-agent in the molten state and the subsequently generated strong residual stress during the quenching process. Since PMMA chains are highly stretched, unlike other conventional crystals which show a three dimensional periodic ordering of atoms or molecules (3D crystallinity), our PMMA exhibits only 1D crystallinity due to ordered lateral packing between chains ($d$ = ~4.3 Å) while the packing is amorphous-like for the other two directions (Scheme 1). When the chains are highly stretched, the lateral packing space becomes regular regardless of stereo-regularity of PMMA chains although the packing spacings in other two directions are dependent on it. Hence, stereo-irregular *a*-PMMAs can be crystallized into 1D hypo-crystalline structure. For the reason of the deficient crystallinity in two axes, we named the crystalline PMMA as 1D hypo-crystalline PMMA (hc-PMMA). Our hc-PMMA crystals are different from the reported paracrystals made of atactic PVC and PAN. Unlike paracrystalline or perturbed regular structures [30], our hc-PMMAs exhibited crystal-like sharp diffraction peaks and clear melting transitions. Additionally, the crystallinity of hc-PMMAs (55–65%) was remarkably higher than that of most paracrystalline structures (<10%), and which cannot be explained by the shape–emulation theory.

## Results

### *Preparation of hc-PMMA films using BA as a chain-stretching agent*

BA was used as a chain-stretching agent in our experiments. As discussed in the next sections, BA stretched PMMA chains by



Please cite this article in press as: J.H. Sim et al., Materials Today (2020), https://doi.org/10.1016/j.mattod.2020.05.003

hydrogen bonding interaction. The molecular details of the various PMMAs used in our experiments are shown in Table S1. Molecular weights of PMMAs ranged from 35 to 1500 kg/mol, which are sufficiently much larger than the conventional entanglement molecular weight ($M_e \approx 10$ kg/mol) [31]. PMMAs were crystallized following the procedures shown in Scheme 1. Briefly, amorphous PMMA powder and crystalline BA powder were mixed together with at a concentration of 5 wt% polymer and ground in an Agate mortar. The powder was then transferred to a clean Si wafer and heated to 150 °C, well above the melting point of BA ($T_m = 122$ °C). The clear solution was then covered with a PDMS film to prevent the evaporation of BA. Once the PMMA and BA were completely mixed/forming a homogeneous clear solution (typically taking less than 5 min), the sample was quickly transferred on the cold metal plate pre-cooled with dry ice/acetone (−78 °C) or with liquid nitrogen (−196 °C). Upon being placed onto the cold plate, the solution was almost instantaneously solidified. BA forms the eutectic system with many polymers including PMMA, PAA (polyacrylic acid), PE (polyethylene) and PES (polyethylene sulfone) [32]. Since BA is in large excess, it may first form pure BA crystals and a polymer-enriched liquid phase which then solidifies at the eutectic composition. To isolate pure hc-PMMA, BA was removed by sublimation under vacuum at 50 °C for 2 days or by immersing in ice-cooled deionized water for 30 h. Complete removal of BA was confirmed by FT-IR and GC (Fig. S1). The resulting hc-PMMA films were white and nontransparent. The hc-PMMAs were completely soluble in common organic solvents such as THF, and their molecular weights measured by GPC were almost same as that of pristine PMMA. These results suggest that there was no chemical crosslinking nor decomposition during the processing.

### *Crystalline PMMAs*

After complete removal of BA, the hc-PMMA films showed strong birefringence when viewed between crossed polarizers in a polarized optical microscope (POM). The films before BA removal also exhibited very strong birefringence, which is presumably mainly because of BA crystals. As shown in Fig. 1a–c, hc-*i*-PMMA, hc-*s*-PMMA and even hc-*a*-PMMA films showed strong birefringence colors. Due to the variation of film thickness, hc-PMMA films exhibited various interference colors by the interplay of birefringence and film thickness [33,34]. Similar birefringence colors were also observed for higher molecular weight PMMAs (Figs. S2 and S3). SEM images showed that hc-PMMA formed microfibrils, highly aligned to a certain direction (Fig. 1d–f). In this case, the direction of microfibrils was consistent with the preferred *b* axis growth direction of BA seen before removing by sublimation. Microfibrils aligned in-plane orientation were mostly found in thin film areas (<20 μm) (Fig. 1e). However, in thicker (>100 μm) regions, the bundles of microfibrils were randomly oriented (Fig. 1f). Due to the random orientation and the weak residual stress (the tensile stress in PMMAs induced by anisotropic crystal growth of BA/PMMA and by large temperature change during quenching), birefringence color was weak or absent in thick films. There were many micropores in the films, which were expected to form during the sublimation of BA, so that micropores are highly elongated parallel to the microfibrils. The PMMA films prepared with other organic crystals including naphthalene, salicylic acid (SA), trimethylbenzoic acid (TMBA), 1,3,5-trichlorobenzene (1,3,5-TCB) and 1,4-dibromotetrafluorobenzene (1,4-DBTFB) did not show birefringence, a polymer melting transition nor the characteristic FT-IR peaks of crystalline PMMAs (will be discussed in the next section).

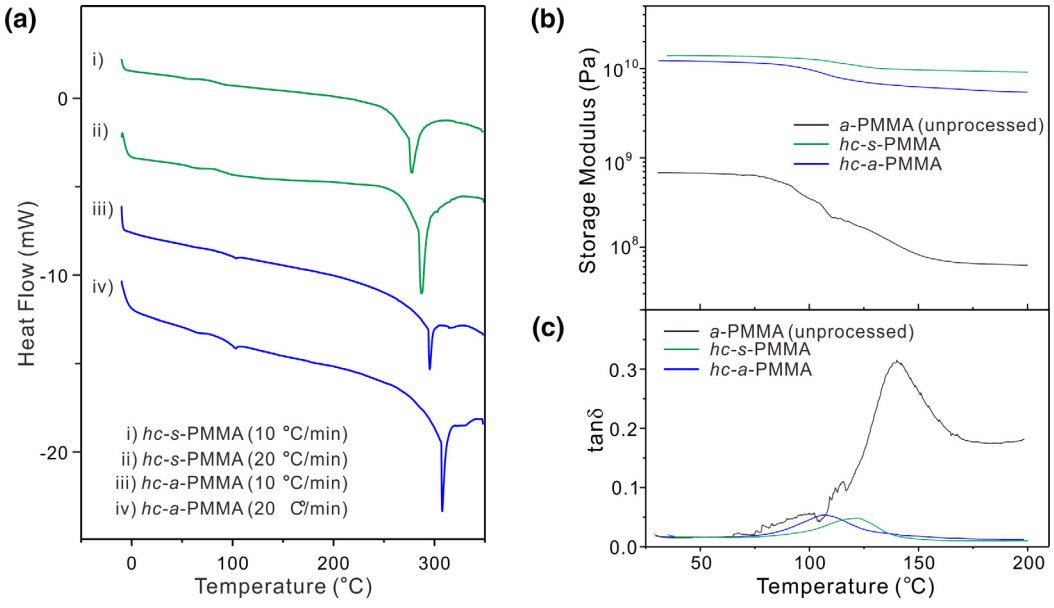


**FIGURE 2**

(a) DSC thermograms of hc-PMMAs at the first heating cycle. (b and c) Powder state DMA measurement of hc-*s*- ($M_n$ = 1500 kg/mol) and hc-*a*-PMMAs ($M_n$ = 120 kg/mol) and unprocessed *a*-PMMA ($M_n$ = 120 kg/mol). DMA measurements were performed from ambient temperature to 200 °C with frequency and amplitude of 1 Hz and 20 μm, respectively. Heating rate was 2 °C/min.



Please cite this article in press as: J.H. Sim et al., Materials Today (2020), https://doi.org/10.1016/j.mattod.2020.05.003

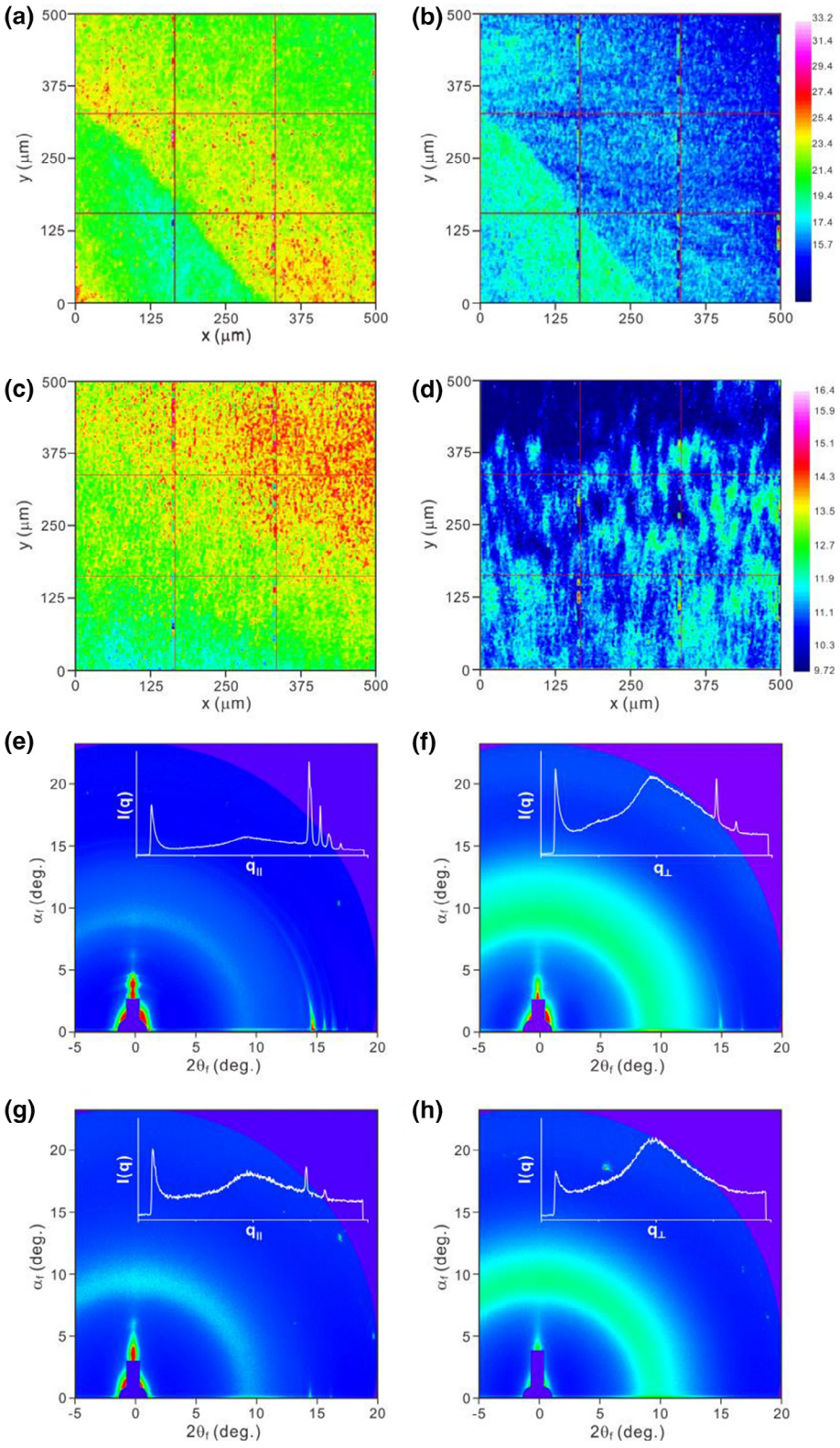


**FIGURE 3**

Polarized FT-IR images of hc-*s*-PMMA ($M_n$ = 35 kg/mol) (a and b) and hc-*a*-PMMA ($M_n$ = 35 kg/mol) (c and d). Polarizer is (a and c) parallel and (b and d) perpendicular to the axis of fibril arrays. For mapping, the absorbance of C═O peak at 1724 $cm^{-1}$ was monitored in the area of 500 × 500 $\mu m^2$. GIXD patterns of (e and f) hc-*s*-PMMA ($M_n$ = 35 kg/mol) and (g and h) hc-*a*-PMMA ($M_n$ = 35 kg/mol). X-ray beam was incident (e and g) parallel and (f and h) perpendicular to the axis of fibril arrays. Insets are in-plane X-ray diffraction profiles, extracted along the $q_y$ direction at $q_z$ = 0.00 $Å^{-1}$.



Please cite this article in press as: J.H. Sim et al., Materials Today (2020), https://doi.org/10.1016/j.mattod.2020.05.003

RESEARCH: Original Research

The crystallization of PMMA was clearly evident by DSC exhibiting distinct clear endothermic transition peaks. As shown in Fig. 2a, DSC thermograms presented a sharp endothermic melting transition peak for hc-*s*-PMMA ($T_m$ = 276.7 ± 0.5 °C, ramp rate = 10 °C/min) and surprisingly even for hc-*a*-PMMA ($T_m$ = 293.8 ± 0.5 °C, ramp rate = 10 °C/min). When the ramp rate increased to 20 °C/min, melting transition peaks were observed at slightly higher temperature ($T_m$ = 283.6 ± 0.5 °C for hc-*s*-PMMA and 306.7 ± 0.5 °C for hc-*a*-PMMA, ramp rate = 20 °C/min), which corresponds to superheating phenomenon [35]. Interestingly, hc-*a*-PMMA exhibited higher $T_m$ than hc-*s*-PMMA. Furthermore, the melting transition peak of hc-*a*-PMMA was narrower than that of hc-*s*-PMMA. This might be related with smaller and more uniform *d*-spacing in hc-*a*-PMMA than that in hc-*s*-PMMA (Tables S3–4). Due to the slightly higher torsional energy barrier of racemic dyads than meso dyads [36], the chain packing in hc-*a*-PMMA that has smaller syndiotactic contents could be more efficient than that in hc-*s*-PMMA. Furthermore, hc-*a*-PMMA retained the stronger residual stress (9.25 GPa) than that of hc-*s*-PMMA (4.48 GPa) by quenching (Table S11) [37]. All these can lead to closer chain packing in hc-*a*-PMMA than hc-*s*-PMMA, and accordingly to the higher melting point. Although direct comparison of $T_m$ between the current system and the previous other studies is not suitable, $T_m$ of hc-PMMAs is significantly higher than melting transitions from previous studies of *i*-PMMA crystals ($T_m$ = 162–220 °C) [27,28,38]. In this case, PMMA decomposition occurred at much higher temperature ($T_d \approx$ 350 °C) (Fig. S4a and b).

Unprocessed neat PMMAs, spin-coated PMMA films (from toluene solution), and PMMA films dissolved at comparable conditions with other low molar mass crystallizable solvents (crystals such as naphthalene, SA, TMBA, 1,3,5-TCB and 1,4-DBTFB) and then quenched did not show the melting transition peak. Additionally, PMMA films (using *i*-, *s*- and *a*-PMMAs) prepared with BA but with slow cooling rate (1 °C/min) and POM-inactive thick samples also did not exhibit the melting transition peak. $T_m$ and heat of fusion ($\Delta H$) data can be found in Table S2. Based on the crystallinity obtained by GIXD which will be discussed in the next section, the fusion enthalpy ($\Delta H_f$) of *s*- and *a*-PMMA was calculated as $\Delta H_f$ = 98.2 J/g and 96.8 J/g, respectively, and which is quite comparable with that of *i*-PMMA ($\Delta H_f$ = 96 J/g) reported elsewhere [38,39]. After melting the hc-PMMAs and bringing the temperature of the melt to 320 °C for 5 min, no re-crystallization transition peak was observed during the cooling, and no melting transition peak could be observed at the second cycle of DSC running (Fig. S4c).

Dramatic enhancement of the mechanical properties of hc-PMMAs further confirms the formation of crystalline structure. To probe the mechanical properties, we used dynamic mechanical analysis (DMA) in the powder state (Fig. S5). The storage modulus ($E'$) obtained from powder DMA tends to be underestimated below $T_g$, and overestimated above $T_g$ comparing with $E'$ obtained from a bulk sample using DMA [40]. As shown in Fig. S5, $E'$ of unprocessed *a*-PMMA ($M_n$ = 120 kg/mol) obtained by powder DMA was $E'$ = 0.67 GPa at room temperature and $E'$ = 0.08 GPa at 150 °C, while bulk film DMA gave $E'$ = 1.62 GPa at room temperature and $E' = 3 \times 10^{-4}$ GPa at 150 °C which are quite comparable to the reported values [41]. Although $E'$ values obtained by powder DMA are different from those by bulk film DMA, the relative comparison among the same set of samples would be still relevant. As shown in Fig. 2b, $E'$ of hc-PMMAs was significantly enhanced comparing with that of unprocessed PMMA. $E'$ of the hc-*s*- and hc-*a*-PMMA ($M_n$ = 1500 and 120 kg/mol, respectively) were measured as $E'$ =14.0 and 12.2 GPa, respectively, which is almost 20 times higher than that of the unprocessed *a*-PMMA ($M_n$ = 120 kg/mol, $E'$ = 0.67 GPa). This large enhancement of $E'$ can be attributed to the crystalline structure of hc-PMMAs. Tan δ also well support crystal formation in hc-PMMAs (Fig. 2c). Tan δ values of hc-PMMAs were much smaller than that of unprocessed neat PMMA, which imparts less amorphous and more crystalline structure in hc-PMMAs. More interestingly, the plateau modulus above $T_g$ ($E_N$) was very high, $E_N$ = 9.7 (hc-*s*-PMMA) and 6.2 GPa (hc-*a*-PMMA) at 150 °C. $E_N$ of the hc-PMMAs were at least two order higher than that of pristine PMMA. The increased $E_N$ in rubbery state is often observed in chemically crosslinked polymers. As mentioned earlier, however, there was no chemical crosslinking in hc-PMMAs. High $E_N$ of hc-PMMAs was attributed to the 1D extension of PMMA chains (discussed in the following sections). Translational diffusion coefficient of polymers decreases as they are stretched. The scaling law for 1D stretched polymer chains is $D \sim N^{-1.5}$ while the Rouse model for coiled polymers gives $D \sim N^{-1}$ [42–44]. Especially, the lateral translational diffusion coefficient ($D_\perp$) which mainly affects decrease of modulus is much smaller than the axial translational diffusion coefficient ($D_\parallel$) for 1D stretched polymer chains [45]. These results suggest that modulus can increase due to the lateral-chain packing crystallinity and 1D chains extension.

### *1-Dimensional crystallinity of hc-PMMAs*

Optical characterization of the BA processed and then sublimed, hc-PMMA films reveals that the PMMA chains regardless of their tacticity are uniaxially well aligned. The polymer chain alignment was probed by polarized FT-IR (Fig. 3a–d) and grazing incidence X-ray diffraction (GIXD) (Fig. 3e–h). Fig. 3a–d show 2D polarized FT-IR mapping images of hc-*s*- and hc-*a*-PMMA films. For mapping, the absorbance of C=O peak at 1724 $cm^{-1}$ was monitored over the area of 500 × 500 $\mu m^2$ with a pixel resolution of 5 μm × 5 μm. The C=O absorbance was strongly dependent on polarization direction of incident radiation. As shown in Fig. 3a and b, the absorbance intensity in hc-*s*-PMMA film was strong when the polarization was parallel to the fibril axis, but it became weak when the polarizer was rotated 90°. These results suggest that the PMMA chains in thin hc-*s*-PMMA films are uniaxially aligned along the fibril direction and parallel to the substrate at the molecular level. Similar polarization dependency of FT-IR intensity was also observed for hc-*a*-PMMA film (Fig. 3c and d). These results are consistent with SEM observation (Fig. 1e) showing the microfibrils are aligned parallel to the substrate.

Fig. 3e–h show GIXD patterns of the hc-*s*- and hc-*a*-PMMA films. Detailed information of samples and patterns including *d*-spacing from horizontal and vertical line-cuts of hc-PMMAs can be found in Figs. S6-S8 and Tables S3–4. Both hc-*s*- and hc-*a*-PMMA films exhibited strong and sharp in-plane diffraction peaks corresponding to *d* = ~4.3 Å when X-ray beam was inci-



Please cite this article in press as: J.H. Sim et al., Materials Today (2020), https://doi.org/10.1016/j.mattod.2020.05.003

dent parallel to the axis of fibril arrays. While diffraction patterns are slightly weaker than hc-*s*-PMMA, surprisingly hc-*a*-PMMA also exhibit clear crystalline diffraction peaks at the slightly shifted position ($d$ = 4.27 and 4.00 Å) from those of hc-*s*-PMMA ($d$ = 4.33, 4.05, 3.88 and 3.65 Å). Except for the broad amorphous halo centered at $d$ = 7.1 Å, no sharp diffraction peaks were observed for the PMMA films prepared by spin-coating or by using other organic crystallizable solvents. Interestingly, diffraction peaks disappeared for hc-*a*-PMMA when the film rotates 90° with respect to original beam incident direction. Diffraction peaks of hc-*s*-PMMA also became significantly weak. For both cases, no out-of-plane diffraction peak was observed. These results suggest that hc-*a*-PMMAs exhibit a type of 1D crystallinity due to ordered lateral inter-chain packing between the oriented chains while the packing is more amorphous-like for the other two directions. The schematic illustration of the possible molecular arrangement of the hc-*a*-PMMA is depicted in Scheme 1b and c. The origin of strong in-plane peaks was attributed to the regular lateral packing of polymer chains along the *x*-axis. In this case, the inter-chain periodicity along the *x*-axis is independent on the tacticity: the longest distance from the methyl ester side groups to the backbone is constant regardless of tacticity (~4.3 Å) (Scheme 1b). This explains why the stereo-irregular *a*-PMMAs can exhibit crystalline structure along the *x*-axis. In contrast, ordering in both *y*- and *z*-directions is highly dependent on the tacticity. Since all *s*- and *a*-PMMAs used in our experiments have more than 20–40% of stereo-irregular content, the ordering in the *y*- and *z*-directions is impeded by the random locations of the side groups (Scheme 1c). Other diffraction peaks with smaller *d*-spacing ($d$ = 4.05, 3.88 and 3.65 Å for hc-*s*-PMMA, and $d$ = 4.00 Å for hc-*a*-PMMA) were attributed to the formation of polymorphs due to the rotation of the methyl ester side groups (Fig. S8). However, the exact crystal structures of hc-PMMAs and their polymorphs are not clear yet.

hc-PMMA is quite similar to the vertically aligned block copolymer lamellar structures. Although their dimension is different, the vertically aligned block copolymer lamellae also show the almost same in-plane-only diffraction patterns in GISAXS [46,47]. The *d*-spacing within hc-PMMA fibrils was 4.3 Å, and much smaller than previously known the *d*-spacing (10.4 and 6.4 Å along the *x*- and *y*-axis, respectively) or the pitch spacing (7.3 Å) of helix structures in *i*-PMMAs (or *i*/*s*-PMMA superhelical structure) [48,49], and average *d*-spacing (6–7 Å, the amorphous halo) of conventional amorphous *a*-PMMAs [29,50]. Based on the peak intensities of GIXD, the 1D crystallinity along *x*-direction was calculated 55–65% for hc-PMMA. It is noteworthy that such high crystallinity of hc-*a*-PMMAs cannot be explained by the shape–emulation theory which was used for the explanation of the crystallinity of atactic PVC and PAN [9,10].

### *BA as chain-stretching agent of PMMA chains in molten solution*

Understanding the PMMA chain conformation in liquid BA is key bringing insight into the origin of the crystallinity of hc-PMMAs. Typical polymer crystals form chain-folded lamellae. To form the 1D lateral chain-chain order, however, PMMA chains should be highly stretched along their main backbone, which is not thermodynamically allowed in the melt state due to large entropy penalty unless there is mechanical tensile strain. To get the picture of the conformation of PMMA chains dissolved in liquid BA, small angle X-ray scattering (SAXS) experiments were performed for PMMA/BA solutions. To our surprise, PMMA chains were highly extended up to 60% of their contour length. Fig. 4a–c show SAXS profiles of the molten solutions of *i*-, *s*- and *a*-PMMA with BA. Porod slope of *i*-, *s*- and *a*-PMMA in *q* range of 0.03–0.1 was 1.5, 1.2, and 1.1 respectively, which suggests a cylindrical shape of PMMA chains [51–53]. Model fitting with the cylinders with polydisperse radius model provided length of stretched chains of approximately up to 60% of contour length of *s*-PMMA ($M_n$ = 35 kg/mol) (Table S5). In this case, several other models including polydisperse Gaussian coil and fractal flexible cylinder were not suitable for fitting (Table S6). Such large extent of elongation of polymer chains in the solution state is highly unusual. While electrostatic repulsion in polyelectrolytes leads to chain-elongation, our zeta-potential measurements prove that the charge generation on PMMA by BA was negligible ($\zeta = -0.51$ mV, 5 wt% *s*-PMMA in BA). At high *q* regime ($q > 0.3$) scattering profiles deviate from cylinder model. The scattering in that regime may be originated from amorphous aggregates in melt solutions.

The pair-distance distribution function ($p(r)$, PDDF) analysis also supports the stretched conformation of PMMA chains more intuitively. PDDFs were obtained from SAXS data (Fig. 4d and Table S7). Unlike typical Gaussian polymer chains in melt/solutions which display a symmetric distribution $p(r)$ profile with single peak, PDDFs of all three molten *i*-, *s*- and *a*-PMMAs with BA showed the asymmetric distribution profiles having a longer tail at larger distance ($r$), and multiple peaks, which strongly suggest that *i*-, *s*- and *a*-PMMA chains are highly stretched forming elongated rod shape in molten BA solutions [52,54]. Such elongated PMMA chains in molten BA solution were also supported by MD simulations (Fig. S9).

PMMA chain stretching in liquid BA is presumably because of hydrogen bonding (H-bond) interaction of BA with PMMA. It is known that H-bond interaction between polymer chains and solvents can lead to chain stretching because energetically favorable H-bond can compensate the loss of conformational entropy of polymers chains. For example, H-bonded PEO chains were more stretched and the more repulsive intermolecular interaction was measured than non-H-bonded one [55]. Since the carboxylic acid group of BA is a good H-bond donor, it forms strong H-bond with the ester groups of PMMA. In this case, the H-bond interaction become more preferential to the extended PMMA chains because of the bulky size of BA. As shown in Fig. S10, the H-bonds are sterically hindered in the kinked-polymer-chain pockets, while H-bonds are easily accessible for the straightened, elongated PMMA chains. Thus the strong preferential H-bond to the extended PMMA chains leads to a fat-cylinder-like structure. To investigate molecule-size dependent H-bond interaction, additional SAXS and solubility tests have been performed using various carboxylic acids (Table S6, Table S10 and Fig. S11). As summarized in Table S10, PMMA was soluble in acetic acid (AA) and propionic acid (PA) as same as in BA, but not soluble in larger carboxylic acid than butanoic acid. While BA consists of more carbon atoms than butanoic acid, its rotational cross-



Please cite this article in press as: J.H. Sim et al., Materials Today (2020), https://doi.org/10.1016/j.mattod.2020.05.003

RESEARCH: Original Research

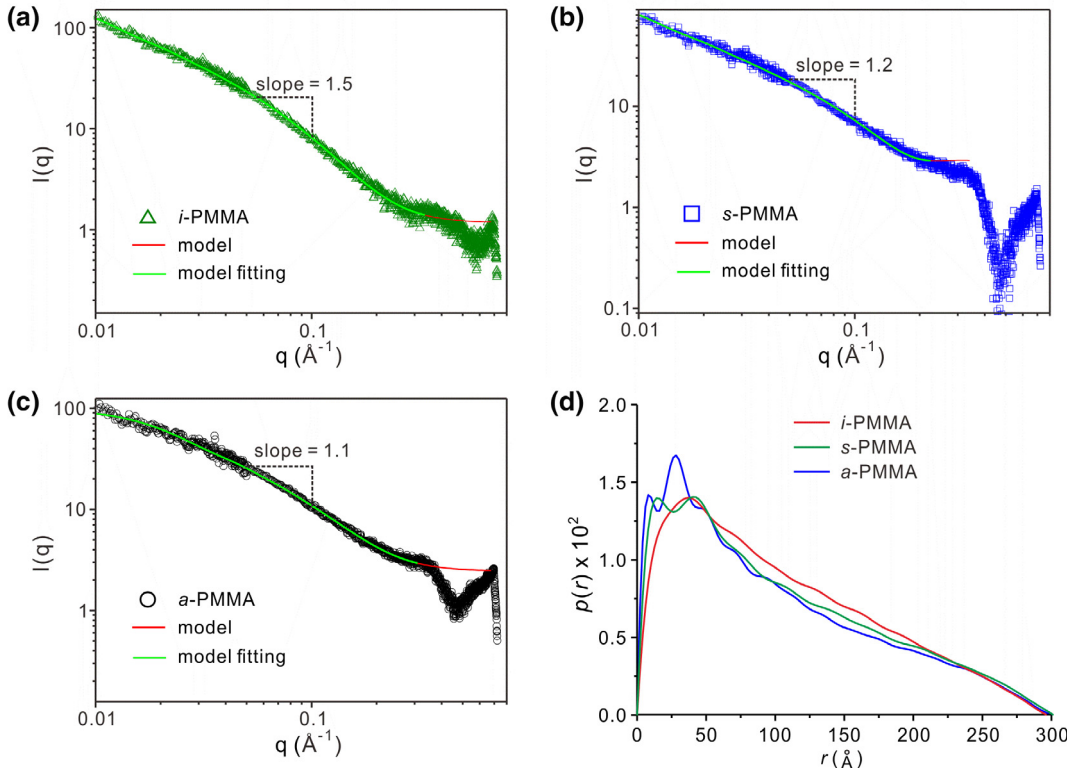


**FIGURE 4**

(a–c) SAXS profiles of PMMA/BA solutions: (a) *i*-PMMA ($M_n$ = 37.2 kg/mol), (b) *s*-PMMA ($M_n$ = 35 kg/mol), and (c) *a*-PMMA ($M_n$ = 35 kg/mol). For SAXS measurements, PMMA was mixed with BA (5 wt%) in a sealed capillary tube, then melted at 150 °C. Red solid line is calculated by the model and green solid line show model fitted line. Cylinder model with polydisperse radius whose form factor with Schulz polydispersity of the cylinder radius was used for model fitting. Porod slopes were obtained by taking a slope in the Prod region ($q$ = 0.03–0.1). (d) PDDFs profiles of PMMA/BA solutions obtained from SAXS data.

section area is smaller than that of butanoic acid but quite similar to that of PA. SAXS analyses show that the Porod slope increased in the order of BA (1.1), PA (1.3) and AA (1.7), which is opposite order of molecule size. Furthermore, cylinder fitting model was well matched for PA as similar as BA, but not suitable for AA (Table S6). Gaussian coil fitting model was suitable for AA. These all results suggest that moderately large size of good H-bond donors can induce the elongation of PMMA chains.

### *Residual stress and squeezing crystallization*

While PMMA chains are highly elongated, no liquid crystalline characteristic was observed for liquid (5 wt%) PMMA/BA solutions at 150 °C, which suggests that long range ordering of PMMA was developed during the quenching process. We think that the crystallization of BA and the residual stress induced by quenching further leads to the formation of hc-PMMAs. For PMMA/BA eutectic system, since BA was in large excess in liquid PMMA/BA solutions, BA will crystallize prior to PMMA, and which makes the remaining PMMA/BA solution enriched in PMMA towards the eutectic composition. In this case, BA formed highly anisotropic acicular crystalline structure even at such high quenching rate, and local temperature gradient makes the BA crystal grow parallel to one another in large area [56]. As illustrated in Scheme 1a, the growing BA crystals can rapidly push PMMA chains outside BA crystals, and force to squeeze PMMA chains. Residual stress is also generated when materials are exposed to fast and large change in temperature. For example, tempered glass is made by rapidly cooling the super-heated glass. During this quenching process, the exterior of glass is solidified by rapid cooling while the interior is cooled relatively slowly, and which induce very large lateral tensile stress inside of the cooled glass. Similarly, it is expected that the residual tensile stress will be applied on PMMA chains when liquid PMMA/BA solutions were quenched (Scheme 1a). In this case, partially elongated PMMA chains by chain-stretching agent in PMMA/BA solution can be further stretched by combination of residual tensile stress and squeezing process during the quenching process, and which led to form hc-PMMA. Since tensile stress by quenching is inversely proportional to the thickness [57], lateral organization of PMMA chains is more preferential for the thinner films. This is well consistent with SEM observations showing laterally well aligned PMMA microfibrils for thin films but the fibrils are oriented in many directions for thick films (Fig. 1).

Residual tensile stress was confirmed by spectroscopic ellipsometry measurements shown in Fig. 5a and Table S11. The theoretical residual stress imposed on hc-PMMAs was calculated by using the stress-optic law, $\Delta n = \Delta c \times \Delta\sigma$ where the relative stress-optic coefficient ($\Delta c$) of PMMA fibers mechanically drawn is $\Delta c = 4.5 \times 10^{-12}$ Pa$^{-1}$ [58]. These results were compared with those of mechanically stretched PMMA films. As shown in Table S11 and Fig. 5a, most of hc-PMMA films presented much larger residual stress than those of mechanically stretched PMMA



Please cite this article in press as: J.H. Sim et al., Materials Today (2020), https://doi.org/10.1016/j.mattod.2020.05.003

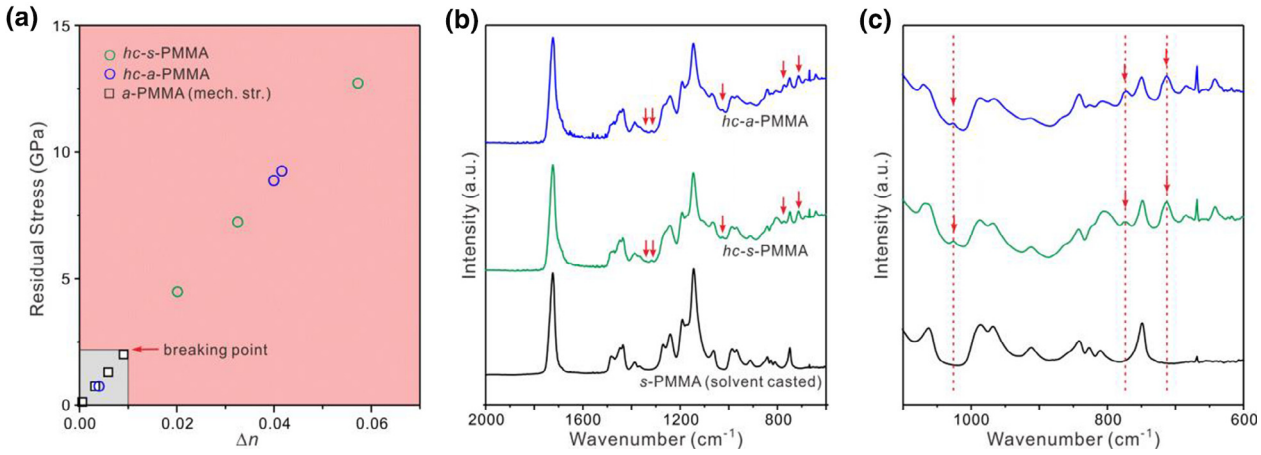


**FIGURE 5**

(a) The residual stress ($\Delta\sigma$) obtained by birefringence ($\Delta n$). Films of hc-*s*- and hc-*a*-PMMAs (shadowed with a pale red) showed much larger $\Delta\sigma$ than the mechanically stretched *a*-PMMA films (shadowed with a gray). The standard deviation of $\Delta n$ and $\Delta\sigma$ was smaller than 5% for all samples. (b and c) ATR FT-IR absorption spectra of hc-*s*-PMMAs, hc-*a*-PMMAs and *s*-PMMA film prepared by spin-casting from a toluene solution. Arrows represent the distinctive peaks of hc-PMMAs. Graphs in (c) is the enlarged region of graphs in (b).

films. While the tensile stress for the mechanically stretched PMMA films approached to the maximum value (~3 GPa) as the strain increased to the breaking point ($\varepsilon = 4.5$), the thermally induced residual stress for hc-PMMAs ranged up to ~13 GPa. In the same context, the reduced strains ($\varepsilon$) of hc-PMMA films were obtained from the strain-birefringence fitting curve of the mechanically stretched PMMA films (Table S11). These results suggest that the large tensile stress which was not obtainable mechanically was applied on hc-PMMA films during the quenching process.

FT-IR spectra also suggest that the tensile bond strain is loaded on the hc-PMMA films. FT-IR spectra of the hc-*s*- and hc-*a*-PMMA films were taken and compared with that of unprocessed PMMA film (Fig. 5b and c). Five distinctive peaks (1340, 1317, 1026, 773 and 713 $cm^{-1}$), which were originated by shift of rocking or wagging peaks of methylene groups in the backbone chains (1387, 1364, 1063, 810 and 749 $cm^{-1}$), were observed in all hc-PMMA films [59]. These peaks were relatively weak, but very consistently appear in both hc-*s*- and hc-*a*-PMMA films with all different molecular weights. The shifted peaks to the lower wavenumber were attributed to the tensile bond strain induced by quenching [60,61]. Same as POM, PMMA films prepared by slow cooling of PMMA/BA solutions or solvent-casted films by toluene didn't exhibited those characteristic peaks in FT-IR. These all results suggest that hc-PMMAs with large residual tensile bond strain formed by quenching of liquid PMMA/BA.

## Discussion

In summary, we have successfully demonstrated the crystallization of *a*-PMMAs forming the 1D hypo-crystal structure by quenching of molten PMMA/BA solutions. In crystallization of PMMA, a chain-stretching agent, BA plays crucial roles that are firstly to elongate PMMA chains up to 60% of the contour length in molten state, and secondly to apply large tensile stress on PMMA chains during the quenching process. We believe that unprecedented stretched cylindrical conformation of PMMA chains in molten BA solution is originated by strong H-bond interaction between carboxylic acid groups of BA and methyl ester groups of PMMA. Due to bulky size of BA, H-bond interactions are preferential to the elongated PMMA chains. Such preferential H-bonding compensate conformational entropy loss of elongated PMMA chains when they are co-melted with BA. Along with the chain-stretching agent, the rapid quenching process is also highly demanded for the formation of hc-PMMAs. Large residual stress is imposed on PMMA chains during rapid quenching of molten PMMA/BA solutions, which helps to further stretch PMMA chains and form 1D crystallinity. Consequently, hc-PMMAs are highly strained and form the uniaxially well organized structure. Because of the uniaxial structure, the periodicity along *x*-axis is regular regardless of tacticity ($d = \sim 4.3$ Å) even if irregular for other two axes. This explains well the origin of crystallinity for the stereo-irregular *a*-PMMAs. Due to 1D crystallization and large residual stress, the mechanical properties of hc-PMMAs have been significantly improved. The storage modulus $E'$ of hc-PMMAs increased by almost 20 times at room temperature. The large $E'$ above $T_g$ was attributed to the decreased diffusion coefficient by chain stretching. The uniaxially well organized PMMA chains are hard to be thermally relaxed due to the difficulty of lateral diffusion.

We anticipate that our crystallization strategy can be extended to other polymer/chain-stretching agent system. Further studies of polymers and their specific chain-stretching agent system will open the possibility finding new route for unprecedented crystalline polymer structures and understanding their mechanical and thermodynamic properties.

## Methods

### *Materials and instruments*

PMMAs with different tacticities and molar masses were purchased from Polymer Source (Dorval, Canada). Benzoic acid (>99.5%), naphthalene (>99%), and 1,3,5-trichlorobenzene (>99%) were purchased from Sigma-Aldrich and used after purifi-



Please cite this article in press as: J.H. Sim et al., Materials Today (2020), https://doi.org/10.1016/j.mattod.2020.05.003

RESEARCH: Original Research

cation by sublimation. All other chemical were purchased from Sigma-Aldrich and used as-received unless stated otherwise. Specification of all PMMAs is summarized in Table S1. Bright field and cross-polarized microscopic images were obtained with Olympus BX51 with TR- N33MU and Nikon D-90 digital camera. Differential scanning calorimetry (DSC) thermograms were obtained with TA Instruments Q20 and Q2000. Measurements were done by two heating rates of 10 and 20 °C/min. The melting temperature ($T_m$) and the heat of fusion ($\Delta H$) were analyzed with TA universal analysis 2000. Approximately 4–5 mg of powder from quenched films were used to obtain thermograms for melting transition and heat of fusion. Approximately 1 mg of powder was used to observe decomposition of samples by thermogravimetric analysis (TGA) with TA instruments SDT-Q600 and Q50. Grazing incidence X-ray diffraction (GIXD), small angle X-ray scattering (SAXS) and polarized FT-IR mapping experiments were performed at Pohang Accelerator Laboratory (PAL) [62]. For GIXD measurements, wavelength, sample to detector distance, and incident angle are 1.12 Å, 224.4 mm, and 0.12°, respectively. Sucrose was used as a reference. For SAXS measurements, a wavelength of 0.73 Å was used and sample-to-detector distance was selected for 4 m and 1 m based on the assumption that maximum length scale of PMMA is contour length ($L$) for the current systems ($q > 2\pi/L \approx 0.01$). Model fitting was performed with IGOR and GNOM. FT-IR spectra were obtained directly from the films using attenuated total reflectance (ATR) FT-IR (Bruker LUMOS) with Germanium tip. Polarized FT-IR spectroscopy measurements were performed by Bruker Hyperion 3000 system with FPA dector. Absorbance mapping was performed against C=O groups in PMMA. Ellipsometry experiments were performed with the RC2-XF spectroscopic ellipsometer (J.A.Woollam Co.) over the wavelength range from 245 to 1000 nm. The birefringence ($\Delta n$) of polymer was defined with the difference between refractive indices in ordinary ($n_o$) and extra-ordinary ($n_e$) axes. $\Delta n$ is related with phase shift ($\delta$) shown in ellipsometry and the birefringence can be obtained by ellipsometry measurements.

$$\delta = \frac{2\pi L(n_o - n_e)}{\lambda} \quad (1)$$

$L$ and $\lambda$ are thickness of film and wavelength, respectively. Incident angle of beam is 65°. $\Psi$ and $\Delta$ were measured at three different angles, namely 0°, 45°, and 90° for films and then all $\Psi$ and $\Delta$ versus $\lambda$ profiles were analyzed by model fitting with Lorentz model. In-plane ($\Delta n_{in}$) and out-of-plane ($\Delta n_{out}$) birefringence were obtained. Model fitting of spectroscopic ellipsometric data was done with CompleteEASE v5.15. Scanning electron microscopy images were obtained with HITACHI S-4800 and FEI Helios 660. Especially for imaging fibrillar structure of hc-PMMA, extremely low acceleration voltage (<1 kV) was applied to get rid of artifacts and beam damage often occurring when imaging non-conductive polymers. Landing voltage (~500 V) was further lowered by applying bias voltage at the sample stage. Dynamic mechanical analysis (DMA) of hc-PMMA and unprocessed PMMA were probed with DMA 8000 (PerkinElmer).

### *Sample preparation*

POM, GIXD, ATR FT-IR, polarized FT-IR, and ellipsometry studies were performed with as-prepared films on Si-wafers. Mechanically stretched *a*-PMMA films in DMA study were prepared by stretching solution-casted films with thickness of 200 μm at 130 °C using universal testing machine (Instron-5569) with 2 kg load cell. For DSC measurements, hc-PMMA films were carefully scratched off the Si substrate and powders were loaded in sample pans. For SAXS experiments, 1:30 mixtures of PMMA and benzoic acid were filled with capillary tubes of 80 × 1.5 mm (length × O.D.) followed by sealing with a micro torch. The liquid solution in the capillary was held at 150 °C using Cu sample holders. For DMA measurements, hc-PMMA films were first prepared with *s*- and *a*-PMMA of molar mass of 1500 and 120 kg·mol$^{-1}$, respectively, as the same procedure done for DSC measurements. The hc-PMMA films were carefully collected by scraping off from the Si substrate using a razor blade. The resulting powders were sandwiched in aluminum material-pockets and loaded on SS/Ti clamp. The reference powdery PMMA sample for DMA was also prepared by scraping off PMMA films from the Si substrate after spin-casting a PMMA/toluene solution. Additionally, self-standing bulk film was prepared by drying 5 wt% PMMA solution in toluene. The size was 10 × 40 mm (width × length) and the thickness was 140 ± 20 μm. Measurements were performed from ambient temperature to 200 °C with frequency and amplitude of 1 Hz and 20 μm, respectively. Heating rate was 2 °C/min.

### *Computer simulation*

The elongation of PMMA chains in molten BA solution was observed by molecular dynamics (MD) simulation method. All the simulation and calculations of various properties of the elongated PMMA chains were done through GROMACS software package version 5.0.4 [63]. To obtain precise results from the MD simulation in polymer dynamics area, one should build a correct amorphous state of the polymers for the system as an initial configuration for the MD simulation. In present work, we built molecular configurations of the PMMA/BA solution through the Amorphous tool in Material Studio (version 7.0) as well as a melt PMMA system to compare each other system. The systems for the PMMA/BA solution contained 50 PMMA chains which have 10 repeating unit, whereas the melt configuration was constructed by 10 PMMA chains. Also, we built the systems for long chains of PMMA with 24 chains and 50 repeating unit. Then the polymer configurations were solvated to make different fraction condition (5, 10, 20, and 30 wt% of the PMMA, and 20 wt% only in long chain case).

All the potential parameters, including the values for the Lennard–Jones potential and electrostatic potential, were from OPLS-AA force field [64]. To handle the computational cost from the long-range electrostatic interactions, they were integrated by Particle Mesh Ewald method [65] and both non-bonded interactions were ignored and shifted to zero value when the interaction ranges are longer than 10 Å.

The process of the MD simulation was done by consecutive calculation steps, in the order of energy minimization, equilibration, and quenching by simulated annealing method. The energy minimization step made the configuration from the above procedure stable to run the MD simulation successfully. We used two energy minimization technique sequentially, first steepest descent method and followed by conjugated gradient



Please cite this article in press as: J.H. Sim et al., Materials Today (2020), https://doi.org/10.1016/j.mattod.2020.05.003

method. These procedure makes a system more stable. The equilibration step was also done by two consecutive processes on NPT ensemble at 420 K and 1 atm. In the first equilibration step, we ran simulation for 10 ns under Bussi-Donadio-Parrinello thermostat [66] and Berendsen barostat [67] with 0.1 ps coupling time. From the result of previous step, another simulation was performed for 10 ns under Nose-Hoover thermostat [68] and Parrinello-Rahman barostat [69,70] with 1 ps coupling time. All simulations were performed with 1 fs of timestep. Once the equilibration step was done, the system quenched to low temperature (200 K) where the temperature was lowered gradually by 20 K. To obtain thermodynamic properties which comes from time-averaging of equilibration states, we quenched the system for 5 ns and equilibrate 5 ns at each temperature range.

To elucidate the elongation of the PMMA chains, we defined a stretching parameter $R_s$ (Eq. (S2)) whose physical meaning is how end-to-end vector of the PMMA chains long compared with fully extended conformation, so 0 means the two end points of the PMMA chains met and 1 means the PMMA chains are fully stretched. Because the $R_s$ parameter shows simply how the two end points are far from each other, it is ambiguous to say that the low value of $R_s$ means the PMMA chains are not stretched in long chain case. So, we also calculated another parameter that accounts how each bond vector correlated with adjacent one, which is the second Legendre polynomial coefficient $P_2$ of cosine of the angle between those vectors (Eq. (S3)). It ranges −0.5 to 1.0; 1.0 means all the vectors aligns fully stretched, 0.0 means random conformation, and −0.5 means all the vectors are orthogonal each other, so it can be said that the $P_2(cos\theta)$ parameter indicates how the polymer chains are linear conformation It is used widely in polymer crystallization area [71].

$$R_s = \frac{\sqrt{< R^2 >}}{R_{max}}, \tag{2}$$

where $R_{max} = nl$

$$P_2(cos\theta) = \frac{3}{2}(< cos^2\theta > -1) \tag{3}$$

## Acknowledgements

This research was supported by Basic Science Research Program through the National Research Foundation of Korea (NRF) funded by the Ministry of Science, ICT & Future Planning (2018K1A3A1A32053991 and 2012R1A6A1029029), and by Samsung Research Funding Center of Samsung Electronics under Project Number SRFC-MA1401-05. X-ray experiments were conducted at 4C, 9A and 12D-IRS beamlines at Pohang Accelerator Laboratory (PAL), Korea. J.H.S. designed and analyzed the experiments. S.E., S.L., C.O., and J.R. assisted with SAXS and GIXD experiments. M.L., S.K. and W.B.L. performed the computational simulations. J.H. obtained the SEM images. D.S. and H.C. helped to analyze DMA and FT-IR data. C.P., and E.L.T. helped to analyze the data and revised the manuscript. Y.K. conceived and supervised the project. J.H.S. and Y.K. are inventors on a patent application (KR 10-2019-0113434) that is related to hc-PMMA.

## Appendix A. Supplementary data

Supplementary data to this article can be found online at https://doi.org/10.1016/j.mattod.2020.05.003.

### References

[1] L. Mandelkern, Crystallization of Polymers: Vol. 2, Kinetics and Mechanisms, Cambridge University Press, 2004.
[2] M. Kutz, Applied Plastics Engineering Handbook: Processing and Materials, William Andrew (2011).
[3] A.D. Rey, E.E. Herrera-Valencia, Biopolymers 97 (2012) 374–396.
[4] S. Kimata et al., Science 316 (2007) 1014–1017.
[5] F. Binsbergen, Nature 211 (1966) 516–517.
[6] P.J. Flory, Trans. Faraday Soc. 51 (1955) 848–857.
[7] G. Natta, P. Corradini, J. Polym. Sci. 20 (1956) 251–266.
[8] P. Rizzo et al., Macromolecules 29 (1996) 8852–8861.
[9] R.J. Hobson, A.H. Windle, Macromolecules 26 (1993) 6903–6907.
[10] R.J. Hobson, A.H. Windle, Macromol. Theory Simul. 2 (1993) 257–262.
[11] P.-G. De Gennes, Scaling Concepts in Polymer Physics, Cornell University Press, 1979.
[12] P.E. Rouse Jr., J. Chem. Phys. 21 (1953) 1272–1280.
[13] M. Zhang et al., Crystals 7 (2016) 4.
[14] T.P. Lodge, Phys. Rev. Lett. 83 (1999) 3218.
[15] S. Stepanow, Phys. Rev. E 90 (2014) 032601.
[16] P. Welch, M. Muthukumar, Phys. Rev. Lett. 87 (2001) 218302.
[17] E. Baer et al., Science 235 (1987) 1015–1022.
[18] H. Wang et al., Science 323 (2009) 757–760.
[19] P.J. Flory, J. Chem. Phys. 15 (1947) 397–408.
[20] L. Mandelkern, Rubber Chem. Technol. 66 (1993) G61–G75.
[21] T. Nakajima et al., Advanced Fiber Spinning Technology, Woodhead Publishing, 1994.
[22] A. Keller, J. Odell, Nature 312 (1984) 98-98.
[23] M. Miles, A. Keller, Polymer 21 (1980) 1295–1298.
[24] Z.-R. Chen et al., Science 277 (1997) 1248–1253.
[25] M.C. Lee, M.A. Golden, J. Elastomers Plast. 20 (1988) 163–186.
[26] T.G. Fox et al., J. Am. Chem. Soc. 80 (1958) 1768–1769.
[27] A. de Boer et al., Polymer 16 (1975) 930–932.
[28] K. Konnecke, G. Rehage, Colloid Polym. Sci. 259 (1981) 1062–1069.
[29] H. Kusanagi et al., Polymer 35 (1994) 2028–2039.
[30] T. Welberry, Rep. Prog. Phys. 48 (1985) 1543.
[31] P.C. Hiemenz, T.P. Lodge, Polymer Chemistry, CRC Press, 2007.
[32] C.V. Funk et al., J. Porous Mater. 16 (2009) 453–458.
[33] W.D. Nesse, Introduction to Optical Mineralogy, Oxford University Press Inc., New York, 2004.
[34] J.H. Yun et al., Polymer 47 (2006) 4831–4838.
[35] B. Wunderlich, Structural data on crystalline polymers by thermal analysis, in: Journal of Polymer Science: Polymer Symposia, Wiley Online Library, 1973, pp. 29–42.
[36] K. Grigoriadi et al., Macromolecules 52 (2019) 5948–5954.
[37] P. Smith, P.J. Lemstra, J. Mater. Sci. 15 (1980) 505–514.
[38] J.M. O'Reilly et al., Macromolecules 15 (1982) 1083–1088.
[39] N.C. Escude et al., Polym. Chem. 3 (2012) 3247–3255.
[40] Tg Comparison of Material Pocket and Bar Sample of Polystyrene (Application Note 007771B_24). Retrieved from Perkin Elmer website: https://www.perkinelmer.com/lab-solutions/resources/docs/APP_007771B_24_Tg_Comparison_of_Material_Pocket_and_Bar_Sample_of_Polystyrene.pdf. Perkin Elmer, Vol. 2019.
[41] J. Brandrup et al., Polymer Handbook, Wiley, New York, 1999.
[42] D. Mukherji et al., Phys. Rev. Lett. 100 (2008) 068301.
[43] T.K. Patra, J.K. Singh, J. Chem. Phys. 140 (2014) 204909.
[44] A. De Virgiliis et al., J. Chem. Phys. 137 (2012) 114902.
[45] K. Zero, R. Pecora, Macromolecules 15 (1982) 87–93.
[46] P. Müller-Buschbaum, A Basic Introduction to Grazing Incidence Small-Angle X-ray Scattering, Springer, 2009.
[47] P. Mueller-Buschbaum, Eur. Polym. J. 81 (2016) 470–493.
[48] E. Yashima, Polymer J. 42 (2010) 3–16.
[49] A.J. Christofferson et al., Chem. Sci. 6 (2015) 1370–1378.
[50] N. Jayakumar et al., Int. J. Mech. Eng. Technol 6 (2015) 139–143.
[51] M. Zhang, A.H.E. Muller, J. Polym. Sci. A 43 (2005) 3461–3481.
[52] C.D. Putnam et al., Q. Rev. Biophys. 40 (2007) 191–285.
[53] Y. Kudo et al., Polym. J. 42 (2010) 812–817.
[54] F. Gröhn, Soft Matter 6 (2010) 4296–4302.

[55] C.-L. Ren et al., J. Phys. Chem. B 112 (2008) 16238–16248.
[56] C. De Rosa et al., Nature 405 (2000) 433–437.
[57] M. Ree et al., J. Appl. Phys. 75 (1994) 1410–1419.
[58] M.K. Szczurowski et al., Opt. Lett. 35 (2010) 2013–2015.
[59] M. Badertscher et al., Structure Determination of Organic Compounds, Springer, Berlin Heidelberg, 2009.
[60] H.A. Willis et al., Polymer 10 (1969) 737–746.
[61] H.-D. Wu et al., Polymer 42 (2001) 4719–4725.
[62] K.-W. Kim et al., Biodesign 5 (2017) 24–29.
[63] H.J. Berendsen et al., Comput. Phys. Commun. 91 (1995) 43–56.
[64] W.L. Jorgensen, J. Tirado-Rives, J. Am. Chem. Soc. 110 (1988) 1657–1666.
[65] T. Darden et al., J. Chem. Phys. 98 (1993) 10089–10092.
[66] G. Bussi et al., J. Chem. Phys. 126 (2007) 014101.
[67] H.J. Berendsen et al., J. Chem. Phys. 81 (1984) 3684–3690.
[68] G.J. Martyna et al., J. Chem. Phys. 97 (1992) 2635–2643.
[69] M. Parrinello, A. Rahman, J. Appl. Phys. 52 (1981) 7182–7190.
[70] S. Nosé, M. Klein, Mol. Phys. 50 (1983) 1055–1076.
[71] G. Reiter, J.-U. Sommer, Polymer Crystallization: Observations, Concepts and Interpretations, Springer Science & Business Media, 2003.





Please cite this article in press as: J.H. Sim et al., Materials Today (2020), https://doi.org/10.1016/j.mattod.2020.05.003